



Measurements of freely-expanding plasma from hypervelocity impacts

N. Lee^{a,*}, S. Close^a, D. Lauben^b, I. Linscott^b, A. Goel^a, T. Johnson^a, J. Yee^a, A. Fletcher^a, R. Srama^c, S. Bugiel^c, A. Mocker^c, P. Colestock^d, S. Green^d

^a Dept. of Aeronautics and Astronautics, Stanford University, Stanford, CA 94305, USA

^b Dept. of Electrical Engineering, Stanford University, Stanford, CA 94305, USA

^c Institut für Raumfahrtssysteme, Universität Stuttgart, Pfaffenwaldring 31, 70569 Stuttgart, Germany

^d Los Alamos National Laboratory, Los Alamos, NM 87545, USA

ARTICLE INFO

Article history:

Received 29 April 2011

Received in revised form

6 October 2011

Accepted 4 January 2012

Available online 13 January 2012

Keywords:

Plasma expansion

Hypervelocity impact

Meteoroid

ABSTRACT

This paper details initial results from a study of electrical effects resulting from hypervelocity impacts at a Van de Graaff dust accelerator. Iron particles between 10^{-15} g and 10^{-10} g in mass were impacted on several different metallic targets at speeds of 1 km/s to 50 km/s. The goal of this study is to characterize the impact-generated plasma and associated RF emission. Results are presented from data collected using retarding potential analyzers. The rate of signal detection was found to have a dependence both on material and on target bias. From a single analyzer, some signal waveforms exhibited oscillatory behavior which is significant in determining the effect of impacts on spacecraft. Using two analyzers at different distances from the target, the expansion speed of the impact plasma was measured to be between 10 km/s and 30 km/s.

© 2012 Elsevier Ltd. All rights reserved.

1. Introduction

Meteoroids routinely impact spacecraft due to their high flux numbers. Although unlikely, meteoroids can damage spacecraft through mechanical or electrical means. While the mechanical damage resulting from a hypervelocity impact has been well-studied, the electrical effects are less well-understood. Note that in this paper we refer to all small, solid, extraterrestrial objects as meteoroids, with no lower limit on size. In experiments performed at the Max Planck Institute for Nuclear Physics (MPIK), we used a Van de Graaff dust accelerator to simulate meteoroid and orbital debris impact events on different metallic targets and to characterize the impact using a suite of RF and plasma diagnostic sensors. Unlike most experiments characterizing impact plasma, we include direct measurements of a freely-expanding plasma from both charged and uncharged targets. Previous studies have typically used an accelerating grid at the target to separate the impact plasma species and focus them into a detector. The grid configuration allows for a straightforward measurement of total charge production but is not representative of a true impact event on a spacecraft. This paper reports initial results from the retarding potential analyzer (RPA) suite used to characterize the expanding impact plasma. These measurements indicate that the plasma

expansion speed from a freely-expanding plasma is consistent with plasma temperatures reported by other experiments, and that spacecraft material and bias must be considered in an analysis of the threat that meteoroids pose to spacecraft electrical systems.

The remainder of this section provides an overview of the electrical failure mechanisms that could be caused by an impact event, examples of hypervelocity impact measurements made in space, and ground-based testing previously performed. Section 2 describes the experiments performed, section 3 presents the results from the RPA suite, and section 4 concludes and outlines our plan for further study.

1.1. Electrical failure mechanisms

Meteoroids and orbital debris range in mass and size from microscopic dust particles up to spent rocket bodies. Since the flux of particles is inversely proportional to the square of the mass, spacecraft are often impacted by meteoroids too small to cause mechanical damage. A small meteoroid traveling at high speed, however, can pose as much of a threat as a larger but slower piece of orbital debris because impact-related electrical effects scale strongly with impact speed. These electrical effects can cause damage to spacecraft systems even if there is not enough mechanical damage to puncture the spacecraft's outer chassis.

A proposed mechanism for RF emission resulting from electron oscillation in an impact-generated plasma is described in detail by

* Corresponding author. Tel.: +1 650 723 3608; fax: +1 650 723 3738.
E-mail address: nnlee@stanford.edu (N. Lee).

Close et al. [1] The general concept is outlined in Fig. 1. Initially, a particle impacts a surface at meteoroid speeds. The kinetic energy of the particle is partially converted to vaporization and ionization energy [2,3]. This results in a small dense plasma formed by ionization of material from both the particle and the target. As the plasma expands it quickly becomes collision-free by dilution. Because of their higher mobility, electrons expand outward faster than ions, creating an ambipolar electric field which pulls the electrons back toward the ions. As the ions expand out more slowly, the electrons oscillate about the ion front due to the ambipolar electric field, radiating at the plasma frequency. This frequency decreases with density as the plasma expands at the isothermal sound speed. The ambipolar electron oscillations cause emission of an electromagnetic pulse (EMP) which takes the form of an RF chirp with the initial frequency dependent on the initial ion density and the rate dependent on density falloff. Note that we have ignored any dust component to the plasma.

A hypervelocity impact could also trigger an electrostatic discharge (ESD) which is a sudden liberation of electrons from the spacecraft surface. This would result in a current pulse and associated EMP with a different spectral signature than one caused by electron oscillation. We believe that these mechanisms provide a potential explanation for spacecraft electrical anomalies and failures due to meteoroid impact. Depending on the type of EMP emitted, some spacecraft systems may be affected more strongly than others.

1.2. In situ evidence

Evidence of electrical effects on spacecraft stem from reported anomalies experienced during meteoroid showers and also from RF measurements on several deep space probes.

At least three spacecraft have been known to experience electrical anomalies during a meteor shower. In 1993, the Olympus spacecraft in geostationary orbit experienced several concurrent anomalies, including a gyroscope shutdown, during the peak of the Perseid meteoroid shower, leading to loss of attitude control and eventual loss of mission [4]. While there was no direct measurement of an impact event (through momentum transfer), the investigation into the anomalies suggested that a meteoroid impact may have triggered an electrical discharge. In 2009, the Landsat 5 spacecraft in low Earth orbit also experienced an attitude anomaly involving a gyroscope during the Perseid shower [5]. In this case, attitude control and regular operation of the satellite was restored. For both spacecraft, it was clear that the anomalies were not due to mechanical damage, since the gyroscopes were returned to operation. During the 2011 Lyrid shower in April, the Advanced Land Observing Satellite “DAICHI” went to a low-power mode and experienced deteriorating power generation [6], and was eventually declared a total loss.

The Cassini spacecraft detected RF signals associated with impact events from nanometer-sized particles which had been

accelerated to 450 km/s [7], and from micrometer-sized particles from Saturn’s rings moving at roughly 10 km/s relative to the spacecraft [8,9]. Broadband electric field measurements were recorded from the 10 m dipole antennas on the Radio and Plasma Wave Science (RPWS) instrument [10–12]. The signals seen during impact events correspond to an ESD pulse followed by decaying oscillations [13]. No known spacecraft anomalies are associated with these impacts.

The STEREO pair of spacecraft have also detected electrical effects of impact events using the STEREO wave instrument (S/WAVES), which are coincident with optical measurements made by the two spacecrafts’ SECCHI instrument suite [14,15]. Additionally, many electrical anomalies with an “unknown catalyst” on-orbit may be attributed to meteoroid impacts.

1.3. Ground-based testing

Many studies have been performed at hypervelocity impact facilities including Van de Graaff dust accelerators, light gas guns, rail guns, and plasma drag accelerators. There has been no complete analysis of the phenomenon of electromagnetic emission from hypervelocity impact, but several previously-reported experiments are particularly relevant to the study of impact-induced electrical effects. Due to the wide span of projectile masses and speeds achievable using different accelerator technologies, the results are often contradictory and are attributed to different physical mechanisms that could be individually dominant for each particular experiment.

Microwave emission has been measured in light gas gun and rail gun experiments by Takano et al. [16–19] They primarily used 1 g polycarbonate projectiles fired at speeds of 1 km/s to 4 km/s into metal plates. Microwave signals were picked up by 2 GHz and 22 GHz horn antennas placed outside the 350 mm diameter vacuum chamber near a window, and appeared to be a random sequence of short pulses. This experiment did not include any plasma characterization, because their proposed mechanism for EM radiation was from microcracking in the target material.

Starks et al. [20] performed a similar experiment seeking RF emission but reported inconclusive results due to extraneous signals from projectile charging as well as from exhaust plasma from the accelerator. This experiment used 900 g titanium flyer plates fired at about 12 km/s through indium foil targets. Unlike the Takano experiments, their RF measurements were taken using DC plates and broadband microwave horns placed inside the chamber behind the foil target.

Crawford and Schultz [21,22] used the two-stage hydrogen light gas gun at the Ames Vertical Gun Range to shoot 0.16 g–0.37 g aluminum spheres into powdered dolomite targets. Impact speeds ranged from 5 km/s to 7 km/s at incidence angles ranging from 15° to 90° relative to the horizontal. Magnetic search coils were used to detect magnetic fields generated by impact plasmas and charge detection plates were used to measure electric current

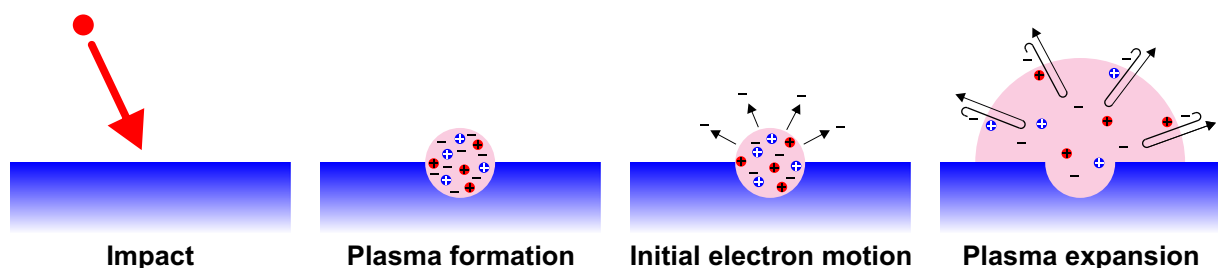


Fig. 1. Depiction of the plasma generation and expansion process due to hypervelocity impact.

as a function of angle and time. This research is unique in that the setup consists of a powdered target, whereas most other hypervelocity impact tests are performed on solid metallic plates.

Putzar et al. [23] have studied the effect of impacts on spacecraft electrical harnesses, but focuses on mechanical damage due to penetration of the spacecraft wall. Their experiment used a light gas gun to fire aluminum spheres with diameters between 1.5 mm and 4.0 mm at speeds of 6.4 km/s to 7.7 km/s. The target included power, data, and RF cable harnesses mounted behind multi-layer insulation. The reported anomalies and failures in the cables were attributed to physical damage, as all impacts resulted in penetration of the structure wall.

The research described above used relatively large projectiles but there has also been a significant number of studies performed at Van de Graaff accelerators, that shoot much smaller particles at higher speeds. In particular, Friichtenicht and Slattery [24] developed the dust accelerator configuration still in operation today and studied impact ionization using a biased target and grounded grid to separate the charges.

Auer et al. [25] used the 2 MV Van de Graaff accelerator at the Max Planck Institute for Nuclear Physics in Heidelberg to study mechanical cratering and penetration as well as electrical charge emission from targets of various materials. The charge collection mechanism was again a series of accelerating grids to separate the positive and negative charges and to direct them into a detector.

Dietzel et al. [26], Dalmann et al. [27], and Göller and Grün [28] also used the Van de Graaff accelerator in Heidelberg to calibrate space-borne dust detectors. These detectors use time-of-flight spectroscopy to analyze the composition of an impact-produced plasma.

Burchell et al. [29] used the 2 MV Van de Graaff accelerator at the University of Kent to fire 10^{-10} g to 10^{-14} g iron particles at aluminum and molybdenum semi-infinite targets in a chamber evacuated to 10^{-6} mbar. Impact speeds were 1 km/s to 42 km/s at an incidence angle of 36° . The targets were charged to 1 kV. Ions were measured using an electron multiplier tube positioned at 90° to the target while a 1.4 kV photomultiplier tube measured the light flash at various other angles of incidence. The energy of the light flash, normalized to projectile mass, was found to be proportional to speed to a power from 3.0 to 3.6 depending on material. They concluded based on the 1 μ s duration of the light flashes that the emission was either from ejecta or the impact plasma, and that it was not due to plasma recombination since it was unaffected by simultaneous plasma measurements using a charged grid. They also concluded based on the measured energy of the plasma that radiant emission is decoupled from its internal energy. Similar tests had been performed at the MPIK facility by Eichhorn [30–33] but with slightly different conclusions. The reported power law for the integrated light flash signal had a speed exponent of 3.8 which was independent of material. Both estimated the temperature associated with the impact flash to be 2500–5000 K, or less than 1 eV.

There is much disagreement in the field about the mechanisms behind impact-induced radiation. Starks et al. [20] attributed impact light flashes to rapid recombination of a fully-ionized plasma, while Burchell et al. [29] concluded that light flashes are not a result of recombination since they were not affected by their direct plasma measurements, which inhibit recombination. Takanô's research group [16–19] associated their microwave signals to microcracking while Starks et al. searched for microwave signals they attributed to plasma oscillation. Crawford and Schultz [21,22] posited a macroscopic charge separation, which may be due to their use of a powdered dolomite target rather than the more commonly studied solid metallic targets.

The disparate test environments that were used is a significant factor in comparing the results from different research groups. In

particular, the achievable vacuum levels at light-gas gun facilities (~ 0.1 mbar) are significantly poorer than at Van de Graaff dust accelerators ($\sim 10^{-5}$ mbar). The effect of ambient atmosphere has been studied for expanding plasma plumes from laser ablation studies [34] and is significant for impact-generated plasmas as well. Most notably, the effect of a collisional ambient atmosphere will suppress free expansion and hence coherent oscillations in the plasma. At the Van de Graaff facilities, where the vacuum level is low enough to representative a spacecraft environment, there has been little research into the production and radiation of RF energy.

2. Experimental approach

Hypervelocity impact experiments were performed at the Max Planck Institute for Nuclear Physics (MPIK). The goal of these experiments was to detect RF emission and to characterize the expanding plasma from impacts using a Van de Graaff dust accelerator. Compared to the previous work described in 1.3, our work maintains the lower vacuum levels achievable at a Van de Graaff dust accelerator but avoids the use of accelerating grids to separate the plasma species. This best replicates the environment seen by an expanding impact plasma after a spacecraft is hit by a meteoroid.

2.1. Facility

The 2 MV Van de Graaff dust accelerator at MPIK is functionally similar to the one described in detail by Burchell et al. [35] and by Mocker et al. [36]. It accelerates positively charged particles from the 2 MV terminal through a series of potential coils and into a vacuum chamber. The speed of the particles is limited by the amount of surface charge that can be accumulated. Since mass drops off faster than surface area, smaller particles tend to be accelerated to higher speeds. A particle selection unit uses induction tubes to measure the charge and speed of particles and capacitor plates to deflect particles not meeting a selection threshold. The mass of particles can be determined from the measured charge and speed by equating the kinetic energy of the particle to the potential energy across the Van de Graaff terminals:

$$\frac{1}{2}mv^2 = qU, \quad (1)$$

where m , v , and q are the mass, speed, and charge of the particle and U is the accelerating voltage.

The vacuum chamber is 1.4 m in diameter and can be depressurized to 10^{-7} mbar. Experiments were performed at pressures between 2.5×10^{-6} mbar and 8.1×10^{-6} mbar, which correspond to a mean free path greater than the size of the chamber. The particle selection unit generates programmable location pulses that are used as trigger signals when the particle is predicted to be at a specified distance downstream from the accelerator.

Spherical iron projectiles were used throughout the experiment. For the impact events analyzed in this paper, the particles span a mass range from 10^{-15} g to 10^{-10} g and a speed range from 2 km/s to 45 km/s. The particle data set and associated cumulative distributions are shown in Figs. 2 and 3.

2.2. Targets

Five different targets were used of varying material and thickness as described in Table 1 and shown in Fig. 4. Except for the aluminum foil target, the other targets are all thick enough to be considered semi-infinite with respect to the projectiles. The brass and copper targets doubled as stub antennas to measure the E-field at the point of impact. The tungsten and two aluminum targets

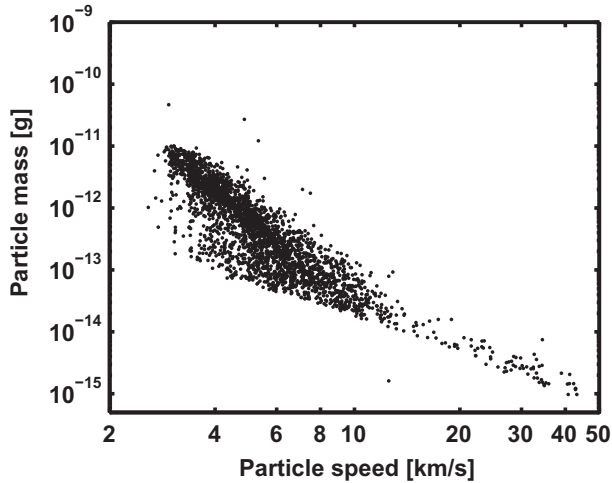


Fig. 2. Distribution of particle masses and speeds. Lower-speed particles are achievable but were deflected by the particle selection unit.

were capable of simulating spacecraft charging using an RC circuit connected to a ± 1 kV voltage source. This RC circuit is composed of a 435 nF capacitor from the target to chamber ground, and a 225 k Ω resistor feeding the capacitor from the voltage source.

The targets were mounted in the chamber at a pitch of 30° up from the horizontal beam line so that the sensors could be aligned more closely with the target normal vector. A mechanical feed-through in the chamber allowed for lateral translation of the target platform to shift each target into the beam line without opening the chamber.

2.3. Sensors

A suite of plasma diagnostic and RF sensors was used to characterize the expanding plasma plume and any emitted RF signal. Results from the RF sensor suite are beyond the scope of this paper but a brief description of the sensors is presented for completeness. The sensor layout is depicted in Fig. 5.

2.3.1. RF sensors

The RF sensor suite is composed of the E-field sensor described above in Section 2.2, two log periodic arrays, and three VLF loop antennas. The E-field sensor includes a built-in amplifier stage at the target and two low-noise amplifier stages outside the chamber. The log periodic arrays were arranged to capture horizontally and vertically polarized signals. Each array had two low-noise amplifier

Table 1
Overview of key target parameters.

	Material	Thickness	Geometry
1	Brass	1 mm	8 mm diameter circle
2	Copper	0.5 mm	40 mm diameter circle
3	Tungsten	0.0508 mm	24 mm \times 26 mm
4	Aluminum	2.70 mm	29 mm \times 29 mm
5	Aluminum foil	0.0127 mm	43 mm \times 16 mm (window)

stages outside the chamber. The three VLF loops were collocated and oriented to measure the magnetic field in three orthogonal directions.

2.3.2. Plasma sensors

Two retarding potential analyzers (RPAs) were positioned near the impact point to measure the expanding plasma plume. The design of the RPA is similar to that described by Marrese et al. [37] and Heelis and Hanson [38]. Each has an effective planar collecting area of 10 cm² behind a sequence of four grids and supported by amplifier electronics. The four grids, from front to back, are the:

1. Floating grid, to shield the internal fields from the incoming plasma;
2. Repeller grid, to select for ions or electrons;
3. Threshold grid, to repel low-energy particles of the selected species; and
4. Suppressor grid, to prevent escape of electrons due to secondary ionization.

For these experiments, the grid voltages were kept low (less than 5 V) to measure the plasma freely impinging on the collecting area. The data show no dependence on grid voltage variations at this level.

The collecting area is connected first to a transimpedance amplifier stage and then to a differential amplifier stage within the RPA housing. This provides a differential signal that is brought out of the chamber on a twisted pair cable. The differential signal is sampled on two separate data acquisition channels. The amplifier electronics and floating grid are grounded to the RPA housing, which is optionally isolated from or grounded to the external chamber ground. The transimpedance gain of the RPA is 16 mV/nA, as determined by a comparison of actual and simulated responses to a test input signal.

The RPAs were placed 75 mm and 150 mm from the impact point (measured to the floating grid), and tilted 15° and 30° off the target normal vector, respectively, as shown in Fig. 5. This

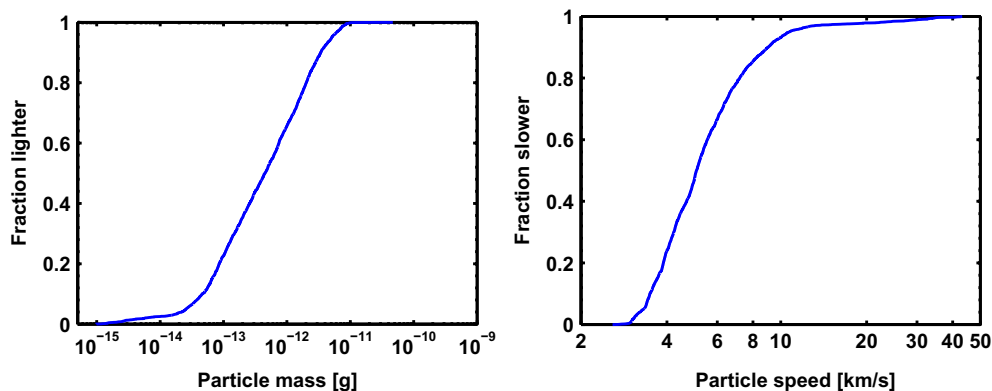


Fig. 3. Left: Cumulative distribution of particle masses. Right: Cumulative distribution of particle speeds.

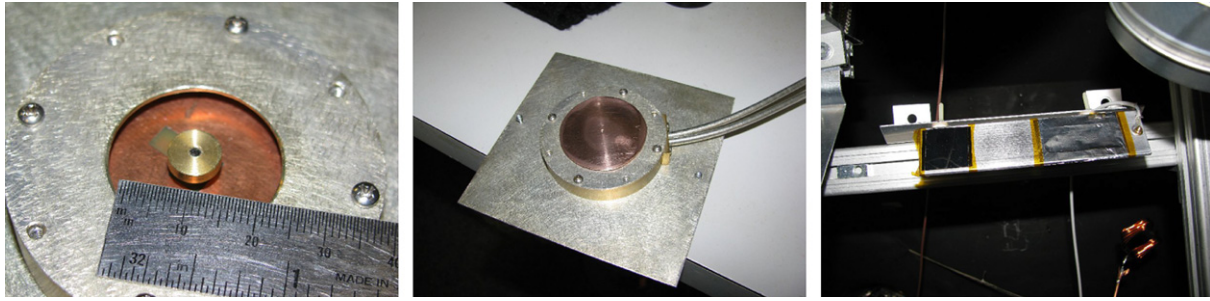


Fig. 4. Left: Brass target. Center: Copper target. Right: Tungsten and aluminum targets.

configuration minimized the angles between the RPAs and the target normal vector, subject to the physical constraints of the RPA housings. The plasma plume is expected to expand primarily along the target normal vector, so the RPAs were arranged to maximize the expected signal. The two RPAs were placed at different distances from the impact point in order to yield a measurement of plasma expansion speed. In the remainder of this paper we will designate the nearer RPA as RPA-A and the further one as RPA-B.

3. Results

A total of 2913 events were recorded where the particle mass and speed could be determined from an inductive pickup loop. From this data set, 1247 events showed a signal peak (evidence of plasma detection) from RPA-A and 92 showed a signal peak from both RPAs using a matched filter. We attribute the much lower detection rate of RPA-B to the focusing effect of the biased targets and the weaker signal produced at the greater distance. Table 2 summarizes the number of events studied by target material and bias. We present a survey of waveform shapes (Section 3.1), an analysis of the frequency content of the signal (Section 3.2), results on the dependence of plasma signal on target material and bias (Section 3.4), and an estimate of impact plasma expansion speed (Section 3.5).

3.1. Plasma signal waveforms

From impacts on unbiased tungsten, several distinctive signal shapes were seen, as plotted in Fig. 6. Some impacts resulted in a fast rise followed by an exponential decay, while other impacts resulted in a gradual rise (on the order of 2–5 μ s). The different signals could be an indication of varying diffusion rates in the expansion front of different impact events. Finally, there were signals with two or more distinct peaks, which could be an indication of electron oscillation or separated ion species.

In Fig. 7, typical signals are shown from impacts on tungsten in the three bias configurations. The signals from positively- and negatively-charged tungsten were similar to the sharply-rising signals from the unbiased tungsten. The signals from negatively-charged tungsten were also negatively polarized, indicating that an excess of electrons were liberated from the target.

Signals from the thick aluminum and aluminum foil targets were similar. Fig. 8 shows typical signals from impacts on aluminum foil in the three bias configurations. Interestingly, the impacts on unbiased aluminum were positively polarized on one day of testing and negatively polarized on a subsequent day. A likely reason for this change is that the unbiased target was floated rather than grounded, and may have accumulated a different amount of charge. As with the tungsten signals, the positively- and negatively-biased aluminum targets produced sharply-rising signals with polarity corresponding to target bias.

Several impact events resulted in signals with oscillatory responses. Fig. 9(a) and (b) show two examples of significant oscillatory behavior in the signal peaks. Each of these signals was the result of an impact speed greater than 20 km/s on a positively-biased target. Out of sixteen impact events greater than 20 km/s on positive targets, eight showed similar oscillations. In contrast, none of the seven impact events greater than 20 km/s on negative targets showed this behavior. Two of the impacts on negative targets, however, included a sustained pulse before the signal decayed, as shown in Fig. 9(c).

The oscillations are attributed to two potential mechanisms: electron oscillation or separation of ion species. In the case of electron oscillation around an ion front, the signal is interpreted as a large positive peak due to ion flux into the detector, with short negative peaks superimposed due to electron flux. In the case of ion separation resulting from different charge-to-mass ratios, the oscillatory signal is caused by separate distinct peaks from different ion species, which would each have differing times of flight to the RPA. Both hypotheses are supported by the lack of oscillatory

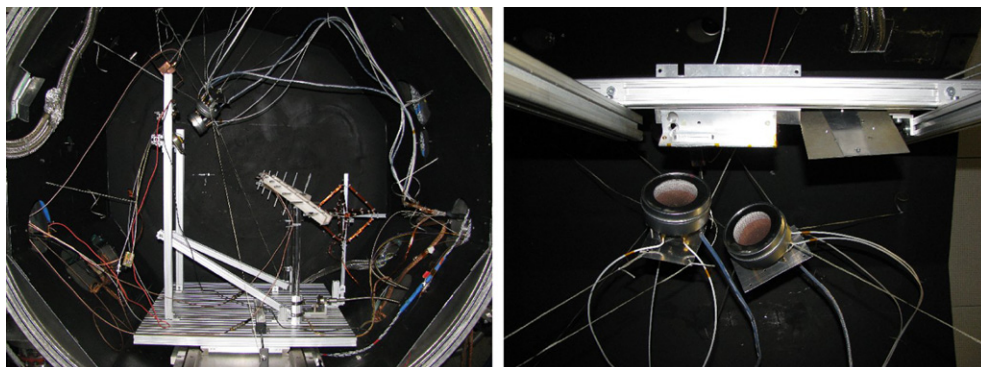


Fig. 5. Left: Layout of the targets and sensors in the vacuum chamber. Right: View looking upward at the targets and RPAs from below.

Table 2

2742 events broken down by target material and bias. A further 171 events occurred on the brass and copper targets, but did not yield a large enough sample of detectable RPA signals to be statistically significant.

		Material		
		W	Al	Al foil
Bias	–1 kV	300	293	188
	Float	628	224	225
	+1 kV	460	215	209

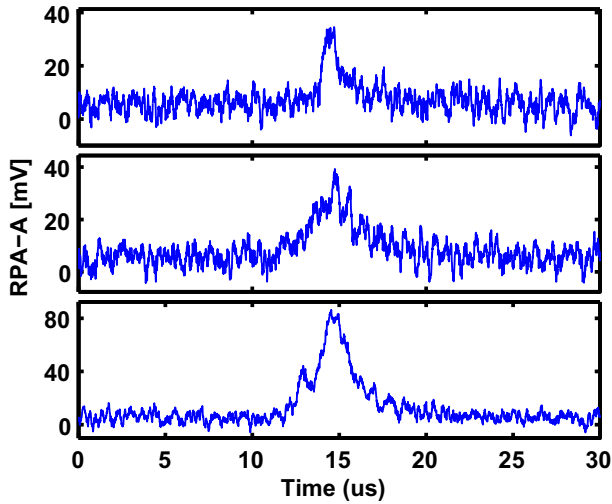


Fig. 6. Signals from RPA-A for impacts on uncharged tungsten. Top: Fast rising and exponential decaying peak from a 4.7 km/s impact of a 1.86×10^{-12} g particle. Middle: Slow rising and falling peak from a 4.1 km/s impact of a 2.62×10^{-12} g particle. Bottom: Oscillatory rise and exponential fall from a 5.2 km/s impact of a 1.91×10^{-12} g particle.

behavior in the negative signals where no ions are present. The waveform shown in Fig. 9(d), however, shows an initial negative signal before the positive, implying the presence of both positive and negative species, rather than discrete pulses of a single species. This signal was generated by a much slower impact but the target

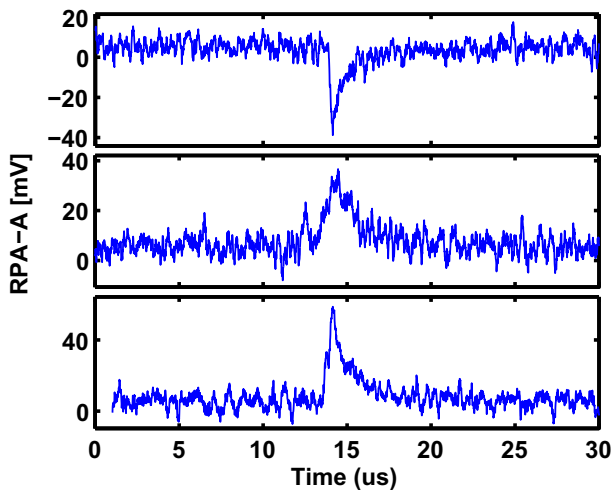


Fig. 7. Signals from RPA-A for impacts on tungsten. Top: Negative sharp peak from a 4.7 km/s impact of a 2.22×10^{-12} g particle on negatively-charged tungsten. Middle: Oscillatory peak from a 3.0 km/s impact of a 7.17×10^{-12} g particle on uncharged tungsten. Bottom: Positive sharp peak from a 3.1 km/s impact of an 8.89×10^{-12} g particle on positively-charged tungsten.

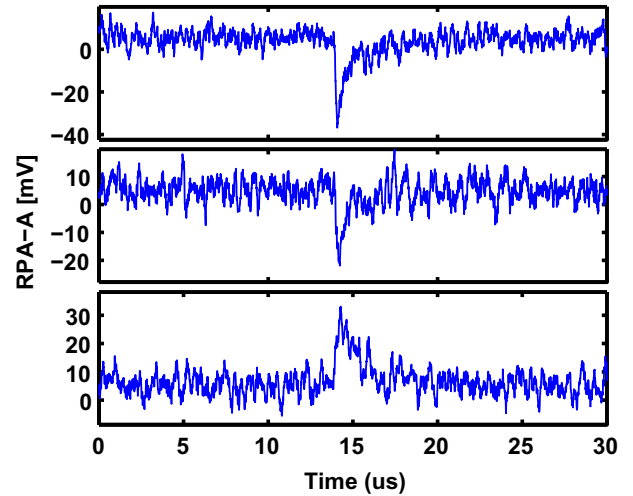


Fig. 8. Signals from RPA-A for impacts on aluminum foil. Top: Negative sharp peak from a 4.0 km/s impact of a 2.40×10^{-12} g particle on negatively-charged aluminum foil. Middle: Negative peak with oscillatory decay from a 6.5 km/s impact of a 1.96×10^{-13} g particle on uncharged aluminum foil. Bottom: Positive sharp peak from a 4.9 km/s impact of a 2.82×10^{-12} g particle on positively-charged aluminum foil.

bias condition was the same as in the oscillatory cases described above. Both mechanisms could potentially be dominant for different impact conditions.

Two other potential mechanisms were considered but rejected as the cause of the oscillations. First, the cyclotron frequency in the test chamber due to the geomagnetic field is estimated to be 1.3 MHz, which is on the order of the oscillation frequency. Second, the peaks could be a result of multiple particle impacts. Smaller particles have a greater tendency to clump in the dust chamber, so it is possible that a cluster of several particles could be accelerated together and drift apart slightly in flight. However, the lack of similar signals in the negatively-charged configuration suggests that the mechanism was not due to either particle clumping or cyclotron behavior.

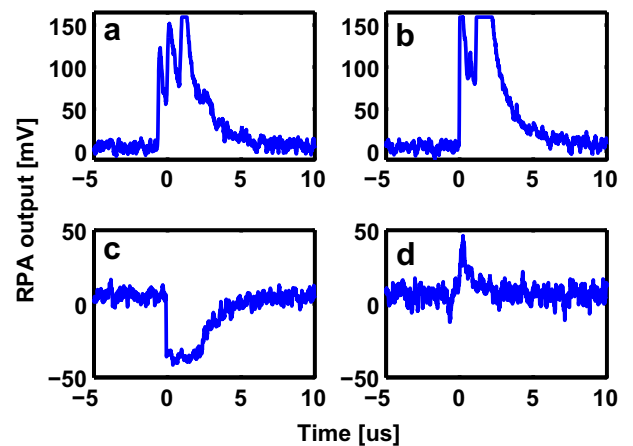


Fig. 9. (a) Signal from RPA-A for a 28.8 km/s impact of a 2.7×10^{-15} g particle on positively-charged tungsten. The signal is saturated at the oscilloscope, not the sensor. (b) Signal from RPA-A for a 34.4 km/s impact of a 7.5×10^{-15} g particle on positively-charged aluminum foil. (c) Signal from RPA-A for a 40.6 km/s impact of a 1.4×10^{-15} g particle on negatively-charged aluminum. (d) Signal from RPA-A for a 3.7 km/s impact of a 3.7×10^{-12} g particle on positively-charged tungsten.

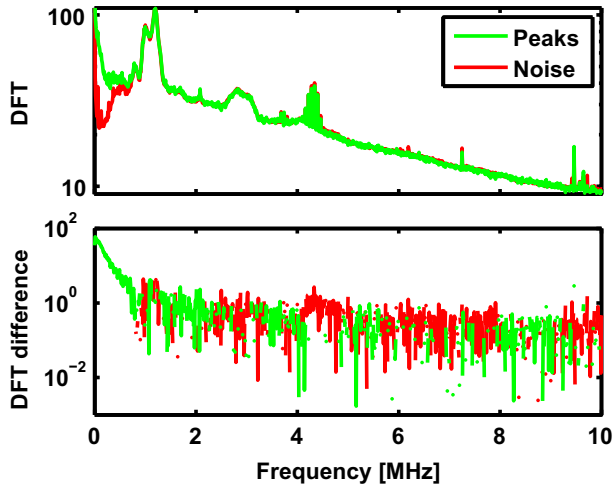


Fig. 10. Top: Averaged discrete Fourier transforms of RPA signals with detectable peaks (in green) and without particles (in red). Bottom: Difference between the averaged discrete Fourier transforms of the signal peaks and the RPA noise, plotted in green when the peak spectrum is greater than the noise and red when the peak spectrum is below the noise. The peak signal is predominantly in the frequency range below 2.5 MHz, but also has components above the noise in several bands around 3.5 MHz and 5 MHz. (For interpretation of the references to colour in this figure legend, the reader is referred to the web version of this article.)

3.2. Plasma signal frequency content

Discrete Fourier transforms (DFTs) of the RPA signals were computed and averaged for events with a detectable plasma peak to produce a cumulative spectrum. A similar averaged DFT was computed for signal traces from the RPA with no impact event to produce a noise spectrum. These average spectra and their difference are shown in Fig. 10. The excess power in the peak spectrum between 1.2 MHz and 2.5 MHz indicates the presence of a discernible signal in this frequency range.

For the signal in Fig. 9(a), a spectrogram (shown in Fig. 11) shows a frequency peak falling from 1.6 MHz to 0.8 MHz. If this is truly a result of electron oscillation and represents a measurement of plasma frequency, then the corresponding plasma density ranges from $3 \times 10^{10} \text{ m}^{-3}$ down to $8 \times 10^9 \text{ m}^{-3}$ as the detectable plume front sweeps over the RPA. This density range is consistent with estimates of the total charge produced by the impact.

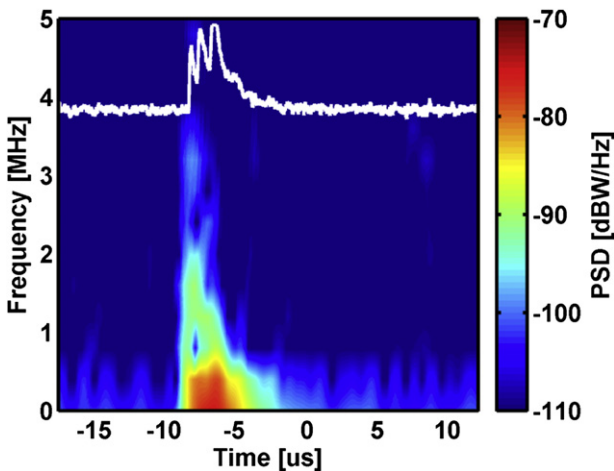


Fig. 11. Spectrogram for the waveform in Fig. 9(a). A 2.5 μs sliding window is used, giving a frequency resolution of 400 kHz.

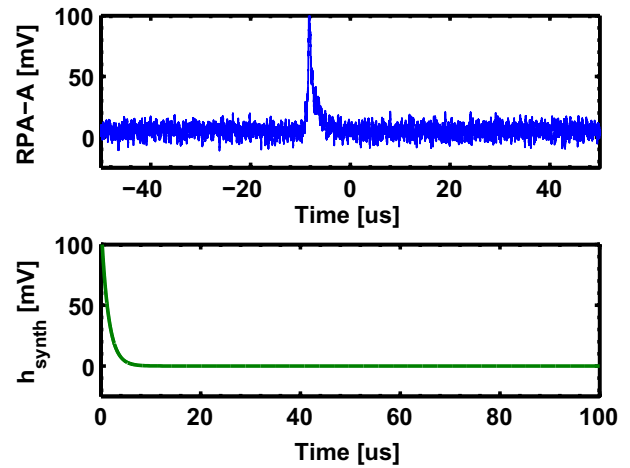


Fig. 12. Top: Signal from RPA-A for a 12.7 km/s impact of a $1.91 \times 10^{-14} \text{ g}$ particle on positively-charged tungsten. This signal was among the sharpest and was selected as the model for the matched filter impulse response. Bottom: Synthetic impulse response constructed by fitting a first-order decaying exponential to the above RPA signal.

3.3. Matched filter

Weak signals were identified using a matched filter with a synthetic impulse response. This impulse response was constructed by fitting a decaying first-order exponential to a strong signal identified from RPA-A. The “canonical” signal pulse and the synthetic impulse response are shown in Fig. 12. The RPA signal from events with large and small signals are shown in Fig. 13 (top and bottom, respectively) with their associated matched filter signal. The matched filter was able to provide identification of signals with all three peak shapes seen and described above.

3.4. Signal detection rate dependence on target

The number of signal peaks detected using the matched filter signal was quantified with respect to target material and bias and is

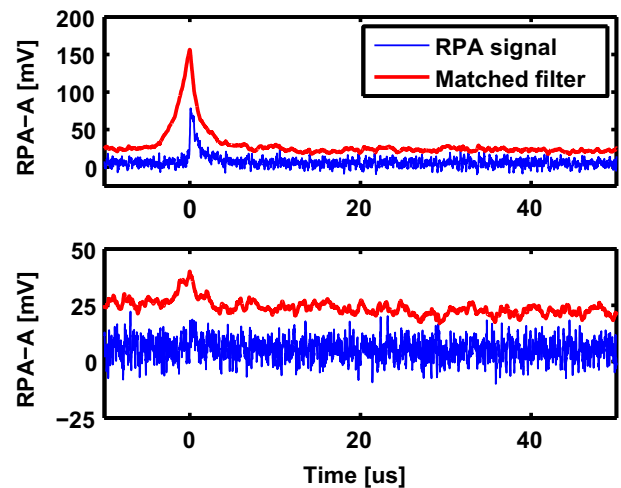


Fig. 13. Signal from RPA-A (in blue) with matched filter output (in red). The matched filter output is scaled by a factor of 1/200 to fit on the axes. Top: A 3.9 km/s impact of a $1.8 \times 10^{-12} \text{ g}$ particle on positively-charged tungsten. Bottom: An 8.7 km/s impact of a $1.5 \times 10^{-13} \text{ g}$ particle on positively-charged aluminum. (For interpretation of the references to colour in this figure legend, the reader is referred to the web version of this article.)

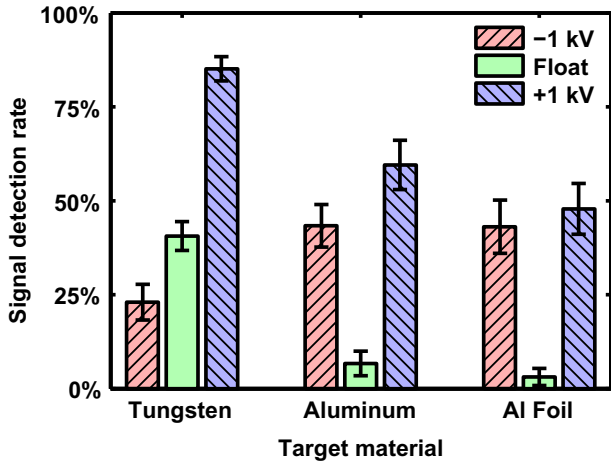


Fig. 14. Percentage of events where RPA signal peaks are detected, out of the set of events with computed particle masses and speeds. Error bars are based on a normal approximation to a binomial process.

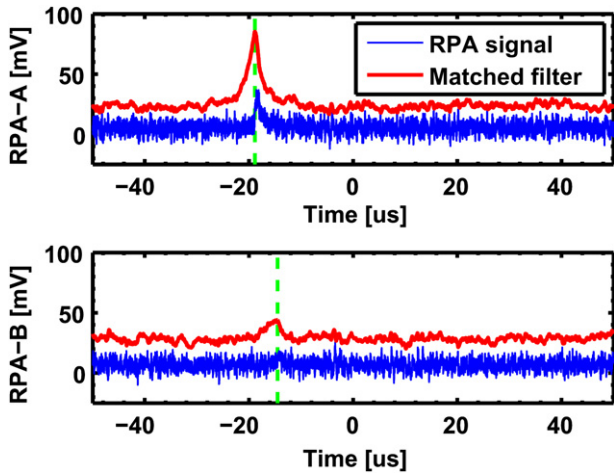


Fig. 15. Signal from both RPAs for a 4.7 km/s impact of a 1.86×10^{-12} g particle on unbiased tungsten (in blue). The output of the matched filter (in red) is scaled by a factor of 1/200 to fit on the axes. The dashed green lines indicate the peaks in each signal, yielding a plasma expansion speed of 17.2 km/s for this event. (For interpretation of the references to colour in this figure legend, the reader is referred to the web version of this article.)

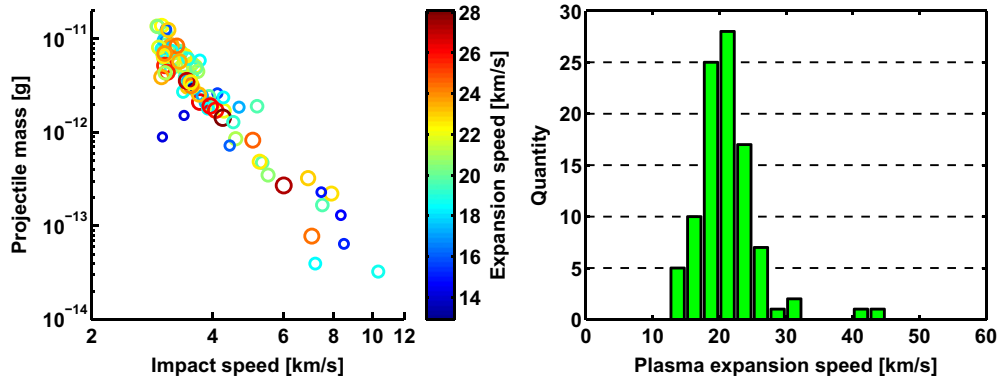


Fig. 16. Plasma expansion speed for impacts on uncharged tungsten. The expansion speed is computed from the time difference between signal peaks in the two RPAs. The expansion speed is indicated by both size and color of each data point.

shown in Fig. 14. While these data do not account for signal strength or any dependence on particle mass and speed, it shows a significant drop in signal detection rate on the two uncharged aluminum targets compared to the uncharged tungsten. However, the detection rate on the negatively-charged tungsten is lower than the rate on either negatively-charged aluminum target. The low detection rates on uncharged targets are understandable — the impact plasma would have a more balanced population of positive and negative species, and would therefore produce a weaker current. However, the reason for the low detection rate on negatively-charged tungsten is unclear. One possible cause is that the geometry of the biased target structure deflected the tungsten-generated electrons in a different direction, since this sample was closest to the edge of the biased structure. This effect would be seen only in the negative case since electrons are more mobile than ions.

3.5. Plasma expansion speed

In order to compute the plasma expansion speed, the temporal difference was measured between the matched signal peaks in the two RPAs, as depicted in Fig. 15. Under the assumption of an isotropic expansion of the plasma plume (within the 30° cone half-angle containing the RPAs), and that the expansion occurs at constant speed, we compute the plasma expansion speed using the baseline range difference of 75 mm. A scatter plot and histogram of expansion speeds resulting from impacts on uncharged tungsten are shown in Fig. 16. Based on these data, the mean expansion speed is 20.8 km/s with a standard deviation of 3.5 km/s. There were not enough data points from the other target configurations to yield a meaningful histogram, but the computed expansion speeds were similar in magnitude to those from uncharged tungsten. While there is some variation in the measured expansion speed, there is no clear dependence of expansion speed on projectile mass or impact speed. However, this result could be an artifact of the mass and speed constraints associated with the Van de Graaff accelerator’s 2 MV operating curve; since there is only a small range of masses that can be accelerated to any given speed, the entire particle distribution could be aligned closely with the level curves of a power law dependence in expansion speed. Assuming that the plasma has reached local thermal equilibrium and that the expansion speed of 20.8 km/s is the plasma isothermal sound speed, the plasma temperature can be computed as a function of ion mass. For ion masses associated with contaminant species (carbon, sodium, and potassium) commonly associated with similar experiments, the plasma temperature is computed to be in the 10 s of eV, consistent with results published by Ratcliff et al. [39].

4. Conclusion

The results presented in this paper describe direct measurements of freely-expanding impact plasma. Oscillatory behavior observed in impacts on positively-charged targets can be attributed either to electron oscillation in a quasineutral plasma or to multiple current pulses because of the times of flight for different ion species. Either mechanism can produce an electromagnetic pulse (EMP) that radiates into the spacecraft, affecting its electrical systems. The power spectrum of the EMP would depend on the behavior of the plasma.

Plasma expansion speeds of 10 km/s to 30 km/s are consistent with other published results and are comparable to predicted speeds based on an isothermal plasma model. This expansion speed indicates that any electrical effect of a hypervelocity impact will be triggered within a very short time after impact before the plasma disperses.

Plasma detection occurred most often from impacts on positively-charged targets, while detection rates for negatively-charged and unbiased targets varied depending on the material. These dependences will be further studied in subsequent testing, with extensions to representative spacecraft materials as well as baseline metallic surfaces.

Based on the results presented here, it appears that the electrical effect of hypervelocity impacts has some dependence on the target material but that the electrical bias state can be more significant. The plasma expansion speed will inform future modeling efforts to refine predicted power spectra emitted by impacts. We conclude that the vulnerability of individual spacecraft systems is highly sensitive to the location of the system within the satellite and to the orientation of the satellite in space, since spacecraft charging is orientation-dependent. Given knowledge of specific electrical systems in a spacecraft, the results presented here could inform future spacecraft designs in order to mitigate the effect of meteoroid impacts on those systems.

Further study is planned at MPIK as well as at a light gas gun facility. Future tests are expected to better characterize the expanding plasma plume geometry, which will yield an improved measurement of plasma expansion speed. In the longer-term we plan to measure in situ meteoroid impact events using a small satellite platform.

Acknowledgment

This study was sponsored by Los Alamos National Laboratory. The authors thank the personnel of the Cosmic Dust Group at MPIK for their support during the experiments.

References

- [1] Close S, Colestock P, Cox L, Kelley M, Lee N. Electromagnetic pulses generated by meteoroid impacts on spacecraft. *Journal of Geophysical Research* 2010; 115(A12328). doi:10.1029/2010JA015921.
- [2] Drapatz S, Michel KW. Theory of shock-wave ionization upon high-velocity impact of micrometeorites. *Zeitschrift Naturforschung Teil A* 1974;29:870–9.
- [3] Gault DE, Heitowitz ED. The partition of energy for hypervelocity impact craters formed in rock. In: *Proc. 6th hypervelocity impact symp.*, vol. 2; 1963. p. 419–56.
- [4] Caswell RD, McBride N, Taylor A. Olympus end of life anomaly – a perseid meteoroid impact event? *International Journal of Impact Engineering* 1995;17(1–3): 139–50. doi:10.1016/0734-743X(95)99843-G. URL: <http://www.sciencedirect.com/science/article/B6V3K-3Y6HS9T-G/2/f5b10be4318027d3547a37aca5c0d359>.
- [5] USGS. Landsat 5 not ready to quit yet. *Landsat Update* 2009;3(4):1. URL: http://landsat.usgs.gov/about_LU_Vol_3_Issue_4.php.
- [6] JAXA. Advanced land observing satellite 'daichi' (alos) power generation anomaly. Press release; 2011.
- [7] Kempf S, Srama R, Horányi M, Burton M, Helfert S, Moragas-Klostermeyer G, et al. High-velocity streams of dust originating from Saturn. *Nature* 2005; 433(7023):289–91.
- [8] Kempf S, Beckmann U, Moragas-Klostermeyer G, Postberg F, Srama R, Economou T, et al. The E ring in the vicinity of Enceladus: I. spatial distribution and properties of the ring particles. *Icarus* 2008;193(2):420–37.
- [9] Srama R, Kempf S, Moragas-Klostermeyer G, Helfert S, Ahrens TJ, Altobelli N, et al. In situ dust measurements in the inner Saturnian system. *Planetary and Space Science* 2006;54(9–10):967–87.
- [10] Kurth W, Averkamp T, Gurnett D. Cassini RPWS observations of dust impacts in Saturn's E-ring. 3600 Bay Area Boulevard. In: *Dust in planetary systems: workshop program and abstracts*, vol. 1280. Houston, TX, 77058-1113, USA: Lunar and Planetary Institute; 2005. p. 102–3.
- [11] Wang Z, Gurnett DA, Averkamp TF, Persoon AM, Kurth WS. Characteristics of dust particles detected near Saturn's ring plane with the Cassini radio and plasma wave instrument. *Planetary and Space Science* 2006;54(9–10): 957–66.
- [12] Meyer-Vernet N, Lecacheux A, Kaiser ML, Gurnett DA. Detecting nanoparticles at radio frequencies: Jovian dust stream impacts on Cassini/RPWS. *Geophysical Research Letters* 2009;36(3):L03103.
- [13] Close S, Kelley MC, Fletcher A, Lee N, Colestock P. RF signatures of hypervelocity impact on spacecraft. In: *3rd AIAA atmospheric space environments conference*. Honolulu, HI: AIAA; 2011.
- [14] Meyer-Vernet N, Maksimovic M, Czechowski A, Mann I, Zouganelis I, Goetz K, et al. Dust detection by the wave instrument on STEREO: nanoparticles picked up by the solar wind? *Solar Physics* 2009;256(1):463–74.
- [15] St. Cyr OC, Kaiser ML, Meyer-Vernet N, Howard RA, Harrison RA, Bale SD, et al. STEREO SECCHI and S/WAVES observations of spacecraft debris caused by micron-size interplanetary dust impacts. *Solar Physics* 2009;256(1):475–88.
- [16] Takano T, Murotani Y, Maki K, Toda T, Fujiwara A, Hasegawa S, et al. Microwave emission due to hypervelocity impacts and its correlation with mechanical destruction. *Journal of Applied Physics* 2002;92:5550.
- [17] Maki K, Takano T, Fujiwara A, Yamori A. Radio-wave emission due to hypervelocity impacts in relation to optical observation and projectile speed. *Advances in Space Research* 2004;34(5):1085–9.
- [18] Ohnishi H, Maki K, Soma E, Chiba S, Takano T, Yamori A. Study on microwave emission due to hypervelocity impact destruction. Delhi: URSI-GA; 2005.
- [19] Ohnishi H, Chiba S, Soma E, Ishii K, Maki K, Takano T, et al. Study on microwave emission mechanisms on the basis of hypervelocity impact experiments on various target plates. *Journal of Applied Physics* 2007;101:124901.
- [20] Starks MJ, Cooke DL, Dichter BK, Chhabildas LC, Reinhart WD, Thornhill III TF. Seeking radio emissions from hypervelocity micrometeoroid impacts: early experimental results from the ground. *International Journal of Impact Engineering* 2006;33(1–12):781–7.
- [21] Crawford DA, Schultz PH. The production and evolution of impact-generated magnetic fields. *International Journal of Impact Engineering* 1993;14(1–4): 205–16.
- [22] Crawford D, Schultz P. Electromagnetic properties of impact-generated plasma, vapor and debris. *International Journal of Impact Engineering* 1999; 23(1):169–80.
- [23] Putzar R, Schaefer F, Lambert M. Vulnerability of spacecraft harnesses to hypervelocity impacts. *International Journal of Impact Engineering* 2008; 35(12):1728–34.
- [24] Friichtenicht JF, Slattery JC. Ionization associated with hypervelocity impact. Tech. Rep. TN-D-2091. NASA; 1963.
- [25] Auer S, Grün E, Rauser P, Rudolph V, Sitte K. Studies on simulated micrometeoroid impact. *Space Research VIII*; 1968:606–16.
- [26] Dietzel H, Eichhorn G, Fechtig H, Grün E, Hoffmann HJ, Kissel J. The HEOS 2 and HELIOS micrometeoroid experiments. *Journal of Physics E: Scientific Instruments* 1973;6(3):209. URL: <http://stacks.iop.org/0022-3735/6/i=3/a=008>.
- [27] Dalmann BK, Grün E, Kissel J, Dietzel H. The ion-composition of the plasma produced by impacts of fast dust particles. *Planetary and Space Science* 1977; 25(2):135–47.
- [28] Göller JR, Grün E. Calibration of the Galileo/Ulysses dust detectors with different projectile materials and at varying impact angles. *Planetary and Space Science* 1989;37(10):1197–206.
- [29] Burchell MJ, Kay L, Ratcliff PR. Use of combined light flash and plasma measurements to study hypervelocity impact processes. *Advances in Space Research* 1996;17(12):141–5.
- [30] Eichhorn G. Measurements of the light flash produced by high velocity particle impact. *Planetary and Space Science* 1975;23(11):1519–25.
- [31] Eichhorn G. Analysis of the hypervelocity impact process from impact flash measurements. *Planetary and Space Science* 1976;24(8):771–6.
- [32] Eichhorn G. Primary velocity dependence of impact ejecta parameters. *Planetary and Space Science* 1978a;26(5):469–71.
- [33] Eichhorn G. Heating and vaporization during hypervelocity particle impact. *Planetary and Space Science* 1978b;26(5):463–7.
- [34] Harilal SS, Bindhu CV, Tillack MS, Najmabadi F, Gaeris AC. Internal structure and expansion dynamics of laser ablation plumes into ambient gases. *Journal of Applied Physics* 2003;93:2380.
- [35] Burchell MJ, Cole MJ, McDonnell JAM, Zarnecki JC. Hypervelocity impact studies using the 2 MV Van de Graaff accelerator and two-stage light gas gun of the University of Kent at Canterbury. *Measurement Science and Technology* 1999;10:41.

- [36] Mocker A, Bugiel S, Auer S, Baust G, Colette A, Drake K, et al. A 2 MV Van de Graaff accelerator as a tool for planetary and impact physics research. *Review of Scientific Instruments* 2011;82:095111. doi:10.1063/1.3637461.
- [37] Marrese CM, Majumdar N, Haas J, Williams G, King LB, Gallimore AD. Development of a single-orifice retarding potential analyzer for Hall thruster plume characterization. IEP-97-066; Cleveland, OH. In: 25th international electric propulsion conference; 1997. p. 397–404.
- [38] Heelis RA, Hanson WB. Measurements of thermal ion drift velocity and temperature using planar sensors. *Measurement Techniques in Space Plasmas: Particles*; 1998:61–71.
- [39] Ratcliff PR, Burchell MJ, Cole MJ, Murphy TW, Alladadi F. Experimental measurements of hypervelocity impact plasma yield and energetics. *International Journal of Impact Engineering* 1997;20(6–10): 663–74.